CHEMISTRY OF MATERIALS
Cite This: Chem. Mater. 2018, 30, 2600−2606
Article
pubs.acs.org/cm

Surface Defect Chemistry and Electronic Structure of $Pr_{0.1}Ce_{0.9}O_{2-\delta}$ Revealed *in Operando*

Qiyang Lu,[†,‡,⊥] Gulin Vardar,[†,§] Maximilian Jansen,[†,§] Sean R. Bishop,[†,‡,#] Iradwikanari Waluyo,[∥] Harry L. Tuller,[‡] and Bilge Yildiz*[,†,‡,§]

[†]Laboratory for Electrochemical Interfaces, Massachusetts Institute of Technology, Cambridge, Massachusetts 02139, United States
[‡]Department of Materials Science and Engineering, Massachusetts Institute of Technology, Cambridge, Massachusetts 02139, United States
[§]Department of Nuclear Science and Engineering, Massachusetts Institute of Technology, Cambridge, Massachusetts 02139, United States
[∥]National Synchrotron Light Source II, Brookhaven National Laboratory, Upton, New York 11973, United States

Supporting Information

ABSTRACT: Understanding the surface defect chemistry of oxides under functional operating conditions is important for providing guidelines for improving the kinetics of electrochemical reactions. Ceria-based oxides have applications in solid oxide fuel/electrolysis cells, thermo-chemical water splitting, catalytic convertors, and red-ox active memristive devices. The surface defect chemistry of doped ceria in the regime of high oxygen pressure, pO_2, approximating the operating conditions of fuel cell cathodes at elevated temperatures, has not yet been revealed. In this work, we investigated the $Pr_{0.1}Ce_{0.9}O_{2-\delta}$ (PCO) surface by *in operando* X-ray photoelectron and absorption spectroscopic methods. We quantified the concentration of reduced Pr^{3+}, at the near-surface region of PCO as a function of electrochemical potential, corresponding to a wide range of effective pO_2. We found that the Pr^{3+} concentration at the surface was significantly higher than the values predicted from bulk defect chemistry. This finding indicates a lower effective defect formation energy at the surface region compared with that in the bulk. In addition, the Pr^{3+} concentration has a weaker dependence on pO_2 compared to that in the bulk.

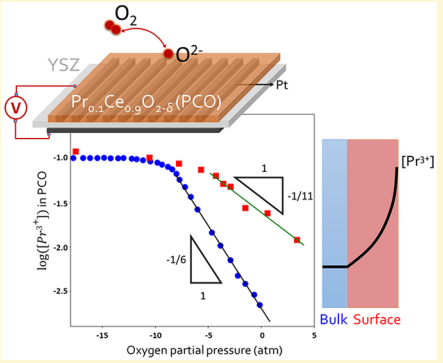

INTRODUCTION

Mixed ionic and electronic conducting (MIEC) oxides based on ceria have been used and studied extensively in clean energy-related applications, ranging from solid oxide fuel/electrolysis cells (SOFC/SOECs)[1−3] to thermo-chemical fuel synthesis[4] to automotive exhaust three-way catalysts (TWCs).[5,6] Recently, ceria-based MIECs have also been explored as candidate materials in resistive switching devices.[7,8] Such memristive devices show promise to become the next-generation memory storage technology, given their potential high packing density and ultralow power consumption.[9] In all of these applications, a deep understanding of defect chemistry is essential in tuning and optimizing the oxygen vacancy concentration to maximize the key figures of merit.[10] Multiple key processes in the applications mentioned above are localized to the surface, including oxygen reduction/evolution reactions and H_2O/CO_2 electrolysis. Quantifying the defect chemistry localized at the near-surface region and relating that to surface reaction kinetics are therefore meaningful and technologically relevant. The bulk defect chemistry for doped and undoped ceria has been well quantified.[11] Obtaining a clear and quantitative assessment of the defect equilibria at the surface region has been more challenging, given difficulties in achieving well-controlled and reproducible atmospheres and electrochemical environments. Earlier studies on nanocrystalline ceria have suggested that large deviations from the defect chemistry characteristic of the bulk exist at the near-surface regions.[12−14] The seminal work reported by Chueh et al.[15] and Feng et al.[16] successfully utilized *in operando* X-ray photoelectron spectroscopy (XPS) to reveal the surface defect concentration of Sm-doped ceria in a reducing H_2/H_2O atmosphere at elevated temperatures. Highly reducing conditions were necessary in those studies to minimize charging issues in the XPS experiments by generation of sufficient electronic conduction. The surface polaron (Ce^{3+} or Ce'_{Ce} in Kröger-Vink notation) concentration was altered either chemically by changing the gas composition or electrochemically by applying an electrical bias. In both cases, the surface polaron concentration was found to be orders of magnitude higher than that in the bulk, which also led to a much higher surface chemical capacitance compared with that of the bulk.[17] While those works covered the regime of reducing conditions, to date there have been no reports on

Received: December 10, 2017
Revised: March 27, 2018
Published: March 27, 2018

DOI: 10.1021/acs.chemmater.7b05129
Chem. Mater. 2018, 30, 2600−2606

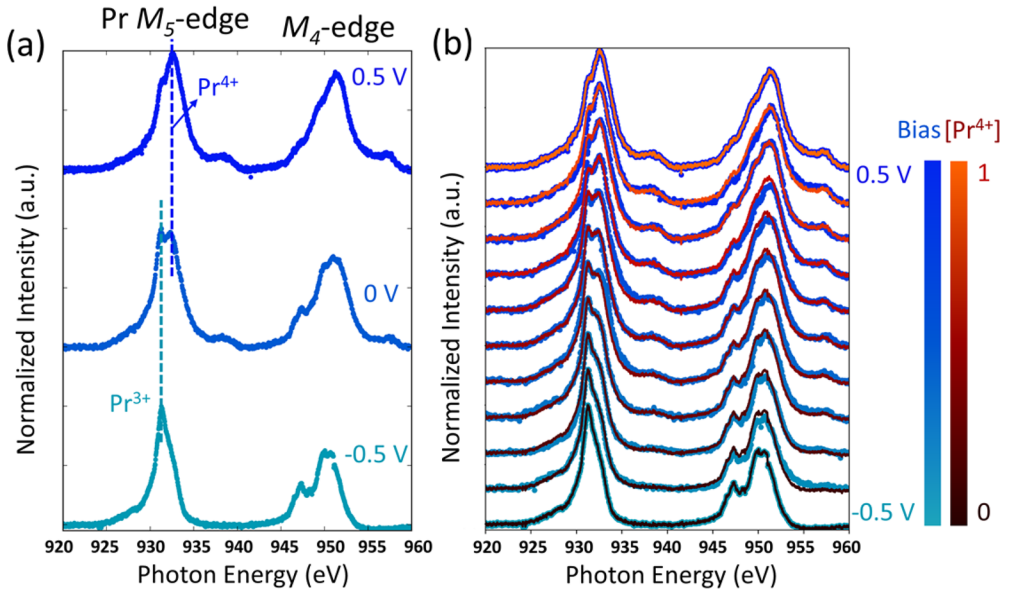

Figure 1. *In operando* Pr $M_{4,5}$-edge X-ray absorption spectra measured at T = 450 °C and pO_2 = 200 mTorr, as a function of applied electrochemical potential on the $(Pr,Ce)O_2$ electrode. (a) Two end-member spectra under ±0.5 V and the spectrum under a 0 V bias, showing that the spectrum at 0 V is a superposition of the two end-member spectra. The dashed lines indicate the peak position of Pr^{3+} and Pr^{4+} oxidation states. (b) Pr $M_{4,5}$-edge spectra in the bias range of −0.5 to 0.5 V. The lines are the linear combination of spectra under −0.5 and 0.5 V, created by choosing the proper Pr^{4+} concentration to reconstruct the data.

the surface defect chemistry equilibria of ceria-based oxides operating in the high-pO_2 oxidizing regime (~1 bar), close to the operating condition for SOFC cathodes or SOEC anodes. This is largely due to the very low electronic conductivity of pure or Sm-doped ceria in this high-pO_2 regime, which in turn hinders the feasibility of the spectroscopic measurements. For resolving the defect chemistry of the surface at high pO_2, praseodymium-doped ceria $[(Pr,Ce)O_{2-\delta}$, denoted as PCO] is an excellent model system. PCO has a relatively high electronic and ionic conductivity, even in the high-pO_2 regime, because of the readily reducible Pr component.[18] Moreover, the bulk defect chemistry,[19] chemical capacitance,[20,21] and chemical expansion properties[22,23] are already well-understood, rendering PCO as an ideal system for contrasting bulk and surface behavior.

In this work, we combine *in operando* ambient-pressure X-ray photoelectron and absorption spectroscopy (XPS and XAS, respectively) with solid state electrochemistry using PCO as the working electrode, to quantify the surface defect chemistry of doped ceria under oxidizing conditions. The electrochemical cell consisted of a PCO thin film deposited on a YSZ single-crystal substrate, with porous Pt as the counter electrode and a dense Pt finger electrode as the current collector. We revealed the surface polaron concentration of PCO at T = 450 °C and pO_2 = 200 mTorr under applied electrochemical potentials ranging from −0.5 to 0.5 V, corresponding to an effective pO_2 range of roughly 10^{-15} to 10^{7} atm. On the basis of Pr $M_{4,5}$-edge XAS, this effective pO_2 range completely covered the oxidation state change of Pr from 3+ to 4+ (i.e., from Pr'_{Ce} to $Pr^{\times}_{Ce}$). We extracted the Pr^{3+} concentration as a function of applied bias, or effective pO_2, by reconstructing the Pr $M_{4,5}$-edge X-ray absorption spectra. As a result, we found that the surface Pr^{3+} concentration deviated significantly from the bulk defect chemistry. More interestingly, the slope of $\log([Pr^{3+}])$ versus $\log(pO_2)$ at the surface was found to be smaller than that derived for bulk defect equilibria. This difference in slope might indicate the presence of strong defect interactions at the near-surface region at such high concentrations of point defects. Alternatively, it may reflect the system achieving minimization of strain energy by segregation of the larger Pr^{3+} ions to the surface, more consequential at overall low Pr^{3+} concentrations under more oxidizing conditions. Finally, we resolved the energy position of Pr defect states in the electronic structure by performing resonant photoelectron spectroscopy.

RESULTS AND DISCUSSION

Quantifying the Pr Oxidation State by *in Operando* X-ray Absorption Spectra. We quantified the Pr oxidation state on a PCO electrode as a function of applied electrochemical potential by measuring and analyzing the Pr $M_{4,5}$-edge spectra, shown in Figure 1. By comparing the Pr $M_{4,5}$-edge X-ray absorption spectra measured under the most oxidizing (0.5 V) and most reducing (−0.5 V) conditions with reference data from the literature,[24] we could confirm that under a 0.5 V bias the Pr cations in PCO were fully in the Pr^{4+} oxidation state, while the Pr cations were switched to fully reduced Pr^{3+} under a −0.5 V bias. The spectra under any bias between −0.5 and 0.5 V could be reconstructed from a linear combination of spectra obtained under 0.5 and −0.5 V, with a variable $[Pr^{3+}]/[Pr^{4+}]$ ratio. The spectrum reconstruction result is shown in Figure 1b, which confirms the good agreement between the measured spectra and the calculated spectra obtained from the linear combination. By using this method, we could extract the Pr oxidation state at different applied electrochemical potentials under *in operando* XAS measurement conditions. We also confirmed that the oxidation state of Ce remained unchanged as Ce^{4+} by measuring Ce 3d X-ray photoelectron spectra throughout the applied electrochemical potential range (see Figure S1).

Surface and Bulk Defect Chemistry of PCO. By using the $[Pr^{4+}]$ fraction used in reconstructing the spectra shown in Figure 1, we could extract the $[Pr^{4+}]$ and $[Pr^{3+}]$ fractions as a

DOI: 10.1021/acs.chemmater.7b05129
Chem. Mater. 2018, 30, 2600−2606

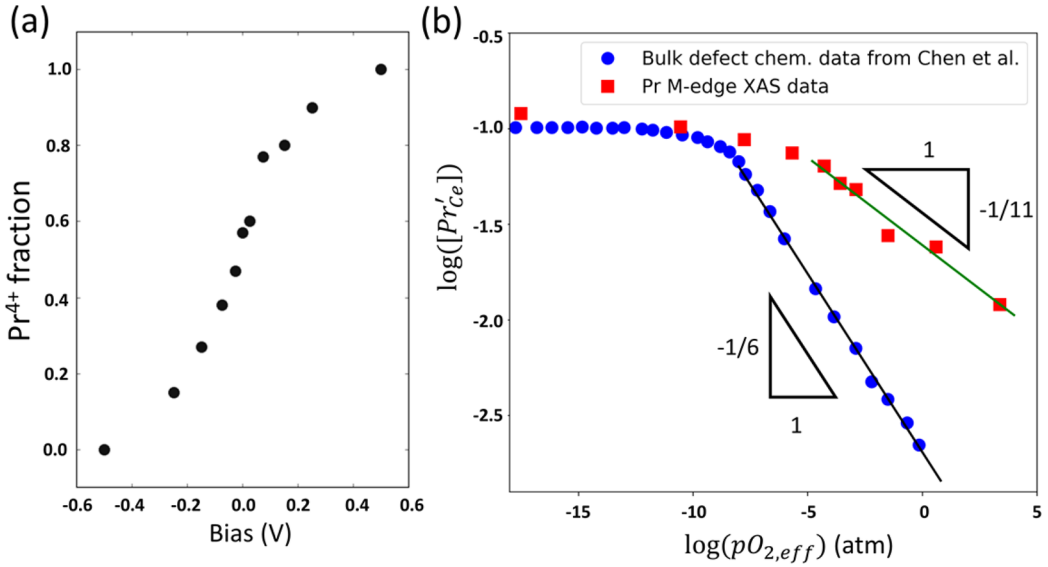

Figure 2. (a) Pr^{4+} fraction, i.e., $[Pr^{4+}]/([Pr^{3+}] + [Pr^{4+}])$, as a function of applied bias. The data points were extracted from spectral reconstruction results shown in Figure 1. (b) Reduced Pr cation concentration [i.e., $[Pr^{3+}]/([Pr] + [Ce])$, shown in Kröger-Vink notation Pr'_{Ce}] as a function of effective pO_2 ($pO_{2,eff}$, calculated from applied bias using the Nernst equation, eq 1). The blue dots are data from ref 20 for bulk defect equilibria in thin film PCO.

function of applied bias on PCO, shown in Figure 2. We convert the applied electrochemical potential, η, to effective oxygen partial pressure $pO_{2,eff}$ by using the Nernst equation:

$$pO_{2,eff} = pO_2 \exp(4e\eta/k_B T) \quad (1)$$

where pO_2 and T are the atmospheric oxygen partial pressure and temperature of the *in operando* measurement condition, respectively (i.e., 200 mTor and 450 °C, respectively), and k_B and e are the Boltzmann constant and unit electron charge, respectively. We assume applied electrochemical η equals the applied electrical bias on the PCO electrode, as discussed in detail below (see Figure 3 and the related text).

We convert the $[Pr^{4+}]$ fraction to the concentration of reduced Pr cations, i.e., the concentration of polarons localized on Pr sites, by using the quantification of surface composition, $[Pr]/([Pr] + [Ce])$, on PCO using XPS (see Figure S3). $[Pr]/([Pr] + [Ce])$ was measured to be around 12%, which is slightly higher than the nominal composition of the PCO target used for thin film deposition ($Pr_{0.1}Ce_{0.9}O_{2-\delta}$). The resulting $[Pr^{3+}]/([Pr] + [Ce])$, denoted in Kröger-Vink notation Pr'_{Ce}, is shown in Figure 2b. It is interesting to compare the surface defect equilibria with the bulk defect equilibria of the nominally same PCO thin films reported by Chen et al.,[20] which are also shown in Figure 2b. One can immediately notice that the surface Pr^{3+} concentration is far higher than that of the bulk, even under highly oxidizing conditions. In both cases, the Pr^{3+} concentration reaches saturation under highly reducing conditions, which is fixed by the Pr dopant concentration. However, as we move toward the higher-pO_2 regime, the surface and bulk defect Pr^{3+} concentrations follow different power law slopes. For the bulk PCO thin films, the $\log([Pr'_{Ce}]) - \log(pO_2)$ plot shows a slope of −1/6, which is well understood based on the defect chemistry model of PCO,[18] i.e., the negatively charged Pr'_{Ce} ions are charge compensated by positively charged oxygen vacancies $V_O^{\cdot\cdot}$. On the contrary, the pO_2 dependence of the Pr'_{Ce} concentration showed a much shallower slope close to −1/11.

This much shallower slope in the $[Pr'_{Ce}]$ versus pO_2 plot on PCO is similar to that found for the $[Ce^{3+}]$ versus pO_2 dependence found for Sm-doped ceria, as reported by Feng et al.[16] However, the conditions for these two observations are highly different. The surface defect chemistry of Sm-doped ceria was probed in a highly reducing H_2/H_2O atmosphere, while this work on PCO was performed over a wide effective pO_2 range, targeting oxidizing conditions. This similarity of surface reduction under vastly different conditions suggests that this phenomenon is more related to the nature of ceria oxide surfaces rather than gas adsorbates under different atmospheres. The observed shallower pO_2 dependence indicates that the surface segregation energy of Pr^{3+} changes as a function of Pr^{3+} concentration, which can be explained by several possible mechanisms. First, one might wonder if this phenomenon can be explained by a space charge layer model, similar to examples found in $SrTiO_3$.[25] In principle, enrichment of oxygen vacancies at the surface can form a positive space charge core, surrounded by an increase in polaron (Pr'_{Ce}) concentration in the space charge zone near the surface. However, the existence of a wide space charge region in such a system with a high dopant concentration is unlikely, because of the very strong screening that is expected. Moreover, earlier work by Chueh et al. on Sm-doped ceria[15] did not find any evidence supporting the existence of space charge layers. An alternative explanation, which we think is more plausible, is the influence of the defect−defect interactions. The level of these interactions in the heavily doped, nondilute systems increases as a function of increasing polaron or oxygen vacancy concentration,[26,27] while assuming local charge neutrality with the coexistence of oxygen vacancies and charge-compensating polarons in the near-surface region.[15,17] Defect interactions and ordering can be more pronounced on oxide surfaces.[28−30] Such defect interactions result in a concentration-dependent formation energy of oxygen vacancies. A larger contribution from defect−defect interactions is expected moving toward more reducing conditions. This effect is expected to be stronger at the surface, so vacancy formation is more significantly suppressed with

DOI: 10.1021/acs.chemmater.7b05129
Chem. Mater. 2018, 30, 2600−2606

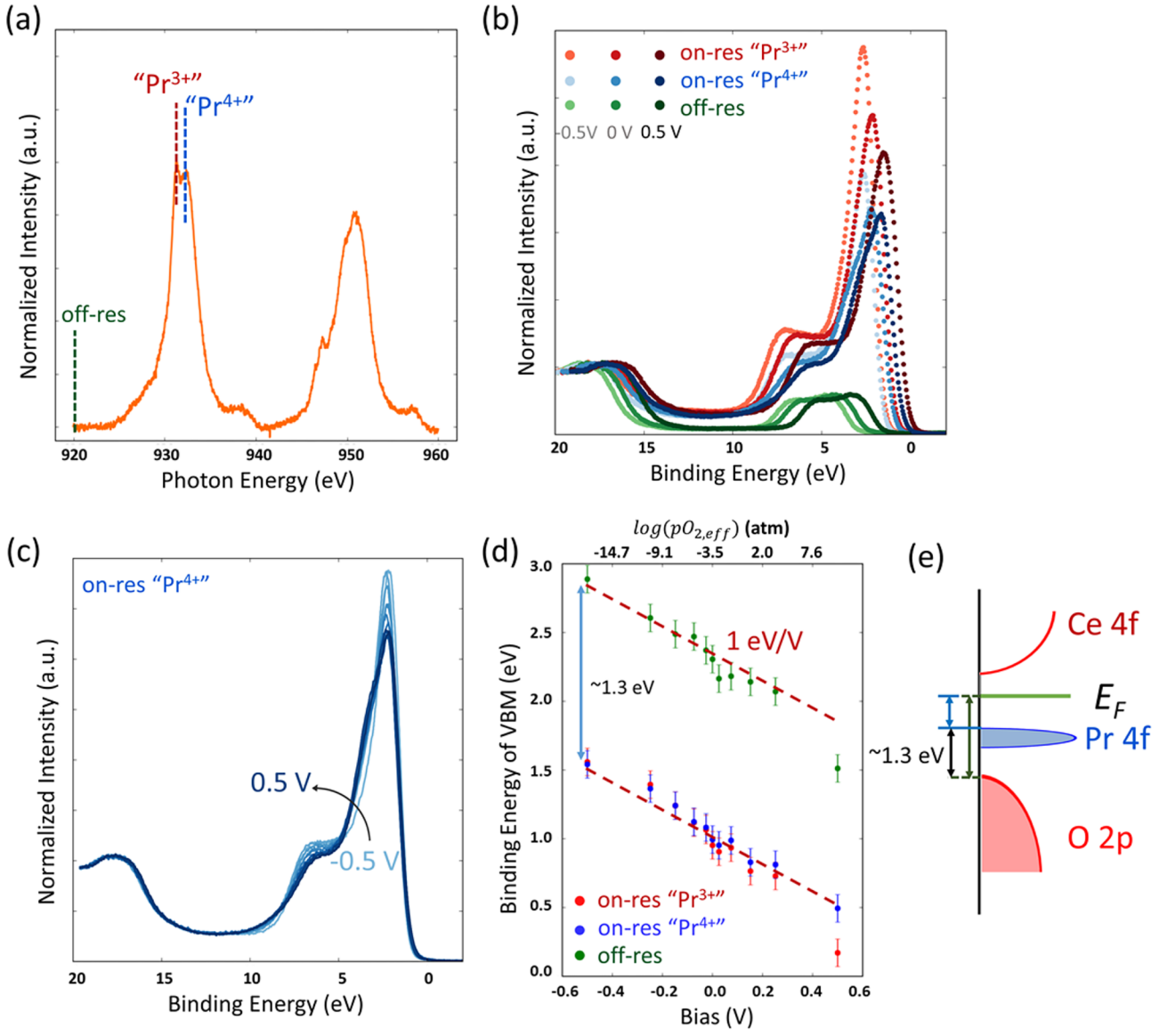

Figure 3. *In operando* resonant photoelectron spectra (RESPES) on PCO. (a) Photon energies selected for RESPES. The off-resonance (off-res) valence band (VB) spectra were collected at an excitation energy before the Pr $M_{4,5}$-edge, while the on-resonance (on-res) VB spectra were measured at photon energies that correspond to the positions of Pr^{3+} and Pr^{4+} XAS peaks. (b) Representative RESPES VB spectra at off-resonance and on-resonance photon energies, under applied biases of −0.5, 0, and 0.5 V. The VB spectra were normalized by the O 2s peak at ∼20 eV. (c) On-resonance VB spectra measured at an excitation energy of 932.6 eV (the maximum XAS peak of Pr^{4+}). The binding energy was shifted to align the Fermi edge, allowing for the comparison of the line shapes. The arrow shows the direction from negative bias to positive bias (reducing → oxidizing). (d) Valence band maxima (VBM) extracted from the RESPES VB spectra, as a function of applied bias. (e) Schematic showing the electronic structure of PCO. The measued 1.3 eV difference represents the distance from the O *2p* band to the Pr *4f* band.

reducing pO_2 than in the bulk, leading to the shallower slope observed. The third possible mechanism for the slope change is the effect of strain energy minimization. Previous studies[31] showed that reduction of Pr^{4+} to Pr^{3+} in PCO causes lattice expansion due to the larger ion radii of Pr^{3+}. It also has been reported that the fraction of Pr^{3+} can be affected by doping with cations of a different ionic radii (for instance Tb) due to the minimization of the strain energy of the whole system.[32] Therefore, the PCO system has a tendency to repel the larger Pr^{3+} ions to the surface to minimize the strain energy, which is similar to the mechanism of surface segregation of alkaline metal dopants reported in perovskite oxides.[33] The level of such surface segregation of dopants with larger diameters as compared with the host cations was shown to decrease with an increase in bulk dopant concentration, as supported by molecular dynamics simulations in our previous study on aliovalent doped ceria.[34] These observations would also explain the smaller difference between surface and bulk Pr^{3+} concentrations under more highly reducing conditions. While several possible mechanisms for the observed weaker pO_2 dependence of Pr^{3+} concentrations at the surface have been suggested, the origin of this slope change, nevertheless, requires further study.

Surface Electronic Structure Probed by Resonant Photoelectron Spectra. We also performed resonant photoelectron spectroscopy near the Pr M_5-edge to resolve the partial density of states (pDOS) of Pr and the energy position of the defect state in the electronic structure of the PCO surface. As

DOI: 10.1021/acs.chemmater.7b05129
Chem. Mater. 2018, 30, 2600−2606

shown in Figure 3a, we measured XPS valence band (VB) spectra at both the off-resonance photon energy before the Pr M_5-edge and on-resonance photon energies at the absorption maxima corresponding to Pr^{3+} and Pr^{4+} oxidation states. Figure 3b shows that the on-resonance VB spectra showed an intensity much higher than that of off-resonance VB spectra, regardless of the applied bias. This enhanced intensity proves the existence of Pr 4f states near the Fermi level,[35−37] consistent with earlier results reported in ref 38. Taking a closer look at the line shape of the on-resonance data, we found that while there were no appreciable changes in on-resonance VB spectra at the Pr^{3+} XAS maximum, clear changes in VB shapes as a function of applied bias were observed for spectra excited at the Pr^{4+} absorption maximum, shown in Figure 3c. This can be explained by the variable Pr^{4+} concentration determined by the applied electrochemical potential, which leads to the change in the pDOS of Pr in the valence band. Future work, including *ab initio* computations, is needed to further clarify the detailed information in the change of pDOS.

From the resonant photoelectron spectra (RESPES) VB spectra, we can also obtain the valence band maxima (VBM) at three different excitation energies, summarized in Figure 3d. We found that the VBM changed with applied bias with a slope of 1 eV/V. This is expected because the applied bias effectively changes the chemical potential of electrons, as also reported in earlier XPS experiments with perovskite[39,40] and fluorite[16] oxides. On the other hand, this also proves that the applied biases are equal to the electrochemical potentials applied to the PCO electrode. More interestingly, we found an ∼1.3 eV difference between the VBM obtained from off-resonance and on-resonance spectra. This difference originates from the distance between O *2p* and Pr *4f* bands, as shown in Figure 3e, because the VB spectra use the Fermi level as the reference point. In the off-resonant VB spectra, O *2p* states dominate the intensity near the VBM. Therefore, the extrapolated VBM indicates the distance from the top of O *2p* states to the Fermi level, while in the on-resonant VB spectra, because the Pr *4f* intensity is much more enhanced, the VBM clearly represents the distance from Pr *4f* states to the Fermi level. By comparing the VBM from both on- and off-resonant spectra, we can extract the distance between O *2p* and Pr 4f states. The measured O *2p*−Pr *4f* distance agrees very well with the earlier value measured by electron energy loss spectra.[41]

CONCLUSIONS

In conclusion, we quantified how the surface defect chemistry of PCO differs from the bulk counterpart by utilizing *in operando* X-ray spectroscopic tools. The surface Pr^{3+} concentration was obtained from the Pr $M_{4,5}$-edge *in operando* XAS data over a wide effective pO_2 range, accessed by applying cathodic and anodic electrochemical potentials, and was found to be significantly higher than that in the bulk at a given pO_2. The much shallower slope of the $\log[Pr'_{Ce}]$ versus $\log pO_2$ dependence for the PCO surface compared with that in the bulk indicated the possible existence of strong defect−defect interactions near the surface or the effect of strain energy minimization. We also probed the change in the Pr-related density of states in the valence band, induced by changes in electrochemical potential, by measuring the valence band spectra on-resonance at the Pr^{4+} absorption maximum. The energy level position of Pr *4f* states probed by RESPES was consistent with previous data measured by electron energy loss spectroscopy.

In our opinion, the implication of the revealed PCO surface defect chemistry is twofold. First, similar to what was reported for Sm-doped ceria under reducing conditions,[15] the surface defect formation energy for PCO is much lower than that of the bulk, even under highly oxidizing conditions. Therefore, one cannot assume that the same defect chemistry model holds when considering surface-limited electrochemical processes. Second, our findings may lend important insights for constructing microkinetic models to better understand the mechanism of oxygen surface exchange reactions. For example, it may no longer be valid to use oxygen vacancy concentrations predicted by bulk defect chemistry equilibria in an attempt to describe surface reaction-limited steps. These new insights related to the surface defect chemistry can be expected to aid in the design of SOFC/SOEC electrodes or active materials for thermo-chemical fuel production with superior performance.

EXPERIMENTAL METHODS

Solid State Electrochemical Cell Fabrication. (100)-oriented single-crystal 8% yttria-stabilized zirconia (YSZ, MTI Corp.) was used as a substrate for fabrication of the $(Pr,Ce)O_{2-\delta}$ electrochemical cell. Pt paste (SPI Supplies) and $(La_{0.6}Sr_{0.4})_{0.95}Co_{0.2}Fe_{0.8}O_3$ (LSCF) paste (Fuel Cell Materials) were mixed and applied onto the backside of YSZ substrates and then annealed at 800 °C in air for 2 h. The resulting porous Pt/LSCF served as the counter electrode of the cell. Patterned Pt dense interdigitated electrodes, with a spacing of 20 μm, were fabricated on the polished side of YSZ substrates as current collectors. A $Pr_{0.1}Ce_{0.9}O_2$ (PCO) thin film was deposited onto Pt/YSZ by pulsed laser deposition with the aid of a KrF excimer laser operating at a wavelength of 248 nm. The substrate temperature and oxygen pressure during deposition were 750 °C and 10 mTorr, respectively.

***In Operando* Ambient-Pressure X-ray Photoelectron and Absorption Spectroscopy (AP-XPS/XAS).** *In operando* AP-XPS/XAS was performed at IOS beamline 23-ID-2 of National Synchrotron Light Source II, Brookhaven National Laboratory. The PCO electrochemical cell was placed on a sample holder equipped with a ceramic heater.[42] The Pt/LSCF counter electrode was grounded to the electron spectrometer with a piece of Pt foil. A portion of the Pt current collected was in contact with K-type thermocouples by using a small piece of Pt foil, which served as the top electrode, while still leaving a large enough area for XPS/XAS measurements. The Pt foil and the K-type thermocouples were pressed down toward the sample surface by a small ceramic spacer held by an Inconel metal clip. A PARSTAT 4000A potentiostat (Princeton Applied Research) was used to apply an electrochemical bias to the electrochemical cell. The AP-XAS measurements were performed using the partial electron yield method. An electron kinetic energy window of around 40 eV centered at 280 eV was used for measuring Pr $M_{4,5}$-edge XAS. For resonant photoelectron spectroscopy (RESPES), the valence band XPS spectra were measured by choosing photon energies both below the Pr M_5-edge ($h\nu$ = 920 eV) and at the Pr M_5-edge XAS peaks corresponding to Pr^{3+} ($h\nu$ = 931.3 eV) and Pr^{4+} ($h\nu$ = 932.6 eV). The photon energies were calibrated by collecting Pt 4f XPS spectra.

ASSOCIATED CONTENT

Supporting Information

The Supporting Information is available free of charge on the ACS Publications website at DOI: 10.1021/acs.chemmater.7b05129.

Ce 3d and O 1s XPS spectra, surface cation stoichiometry, and Pr $M_{4,5}$-edge XAS spectra simulated by using CTM4XAS (PDF)

AUTHOR INFORMATION

Corresponding Author

*E-mail: byildiz@mit.edu.

DOI: 10.1021/acs.chemmater.7b05129
Chem. Mater. 2018, 30, 2600−2606

ORCID

Qiyang Lu: 0000-0002-9155-3684

Iradwikanari Waluyo: 0000-0002-4046-9722

Present Addresses

[⊥]Q.L.: Oak Ridge National Laboratory, Oak Ridge, TN 37831.

[#]S.R.B.: Redox Power Systems, College Park, MD 20742.

Notes

The authors declare no competing financial interest.

■ ACKNOWLEDGMENTS

The authors acknowledge the funding support from the Massachusetts Institute of Technology (MIT) MRSEC through the MRSEC Program of the National Science Foundation (NSF) under Grant DMR-1419807. The authors also acknowledge the use of the Center for Materials Science and Engineering, an MRSEC facility of the NSF at MIT. This research used beamline 23-ID-2 of the National Synchrotron Light Source II, a U.S. Department of Energy (DOE) Office of Science User Facility operated for the DOE Office of Science by Brookhaven National Laboratory under Contract DE-SC0012704.

■ REFERENCES

(1) Chen, D.; Bishop, S. R.; Tuller, H. L. Praseodymium-Cerium Oxide Thin Film Cathodes: Study of Oxygen Reduction Reaction Kinetics. *J. Electroceram.* **2012**, *28*, 62−69.

(2) Chueh, W. C.; Haile, S. M. Electrochemistry of Mixed Oxygen Ion and Electron Conducting Electrodes in Solid Electrolyte Cells. *Annu. Rev. Chem. Biomol. Eng.* **2012**, *3*, 313−341.

(3) Chueh, W. C.; Hao, Y.; Jung, W.; Haile, S. M. High Electrochemical Activity of the Oxide Phase in Model ceria−Pt and ceria−Ni Composite Anodes. *Nat. Mater.* **2011**, *11*, 155−161.

(4) Chueh, W. C.; Falter, C.; Abbott, M.; Scipio, D.; Furler, P.; Haile, S. M.; Steinfeld, A. High-Flux Solar-Driven Thermochemical Dissociation of CO_2 and H_2O Using Ceria Redox Reactions. *Science* **2010**, *330*, 1797−1801.

(5) Bernal, S.; Blanco, G.; Calvino, J. J.; Gatica, J. M.; Omil, J. A. P.; Pintado, J. M. Characterisation of Three-Way Automotive Aftertreatment Catalysts and Related Model Systems. *Top. Catal.* **2004**, *28*, 31−45.

(6) Boaro, M.; Trovarelli, A.; Hwang, J.-H.; Mason, T. O. Electrical and Oxygen Storage/release Properties of Nanocrystalline Ceria−zirconia Solid Solutions. *Solid State Ionics* **2002**, *147*, 85−95.

(7) Schweiger, S.; Pfenninger, R.; Bowman, W. J.; Aschauer, U.; Rupp, J. L. M. Designing Strained Interface Heterostructures for Memristive Devices Materials Theory. *Adv. Mater.* **2017**, *29*, 1605049.

(8) Schweiger, S.; Kubicek, M.; Messerschmitt, F.; Murer, C.; Rupp, J. L. M. A Microdot Multilayer Oxide Device: Let Us Tune the Strain-Ionic Transport Interaction. *ACS Nano* **2014**, *8*, 5032−5048.

(9) Waser, R.; Dittmann, R.; Staikov, G.; Szot, K. Redox-Based Resistive Switching Memories - Nanoionic Mechanisms, Prospects, and Challenges. *Adv. Mater.* **2009**, *21*, 2632−2663.

(10) Tuller, H. L.; Bishop, S. R. Point Defects in Oxides: Tailoring Materials Through Defect Engineering. *Annu. Rev. Mater. Res.* **2011**, *41*, 369−398.

(11) Tuller, H. L.; Nowick, A. S. Defect Structure and Electrical Properties of Nonstoichiometric CeO_2 Single Crystals. *J. Electrochem. Soc.* **1979**, *126*, 209−217.

(12) Kim, S.; Maier, J. On the Conductivity Mechanism of Nanocrystalline Ceria. *J. Electrochem. Soc.* **2002**, *149*, J73−J83.

(13) Kim, S.; Merkle, R.; Maier, J. Oxygen Nonstoichiometry of Nanosized Ceria Powder. *Surf. Sci.* **2004**, *549*, 196−202.

(14) Knauth, P.; Engel, J.; Bishop, S. R.; Tuller, H. L. Study of Compaction and Sintering of Nanosized Oxide Powders by in Situ Electrical Measurements and Dilatometry: Nano CeO_2—case Study. *J. Electroceram.* **2015**, *34*, 82−90.

(15) Chueh, W. C.; McDaniel, A. H.; Grass, M. E.; Hao, Y.; Jabeen, N.; Liu, Z.; Haile, S. M.; McCarty, K. F.; Bluhm, H.; El Gabaly, F. Highly Enhanced Concentration and Stability of Reactive Ce^{3+} on Doped CeO_2 Surface Revealed in Operando. *Chem. Mater.* **2012**, *24*, 1876−1882.

(16) Feng, Z. A.; El Gabaly, F.; Ye, X.; Shen, Z.-X.; Chueh, W. C. Fast Vacancy-Mediated Oxygen Ion Incorporation across the Ceria−gas Electrochemical Interface. *Nat. Commun.* **2014**, *5*, 4374.

(17) Gopal, C. B.; El Gabaly, F.; McDaniel, A. H.; Chueh, W. C. Origin and Tunability of Unusually Large Surface Capacitance in Doped Cerium Oxide Studied by Ambient-Pressure X-Ray Photoelectron Spectroscopy. *Adv. Mater.* **2016**, *28*, 4692−4697.

(18) Bishop, S. R.; Stefanik, T. S.; Tuller, H. L. Electrical Conductivity and Defect Equilibria of $Pr_{0.1}Ce_{0.9}O_{2-\delta}$. *Phys. Chem. Chem. Phys.* **2011**, *13*, 10165−10173.

(19) Chen, D.; Bishop, S. R.; Tuller, H. L. Nonstoichiometry in Oxide Thin Films Operating under Anodic Conditions: A Chemical Capacitance Study of the Praseodymium-Cerium Oxide System. *Chem. Mater.* **2014**, *26*, 6622−6627.

(20) Chen, D.; Bishop, S. R.; Tuller, H. L. Non-Stoichiometry in Oxide Thin Films: A Chemical Capacitance Study of the Praseodymium-Cerium Oxide System. *Adv. Funct. Mater.* **2013**, *23*, 2168−2174.

(21) Chen, D.; Tuller, H. L. Voltage-Controlled Nonstoichiometry in Oxide Thin Films: $Pr_{0.1}Ce_{0.9}O_{2-\delta}$ Case Study. *Adv. Funct. Mater.* **2014**, *24*, 7638−7644.

(22) Bishop, S. R.; Marrocchelli, D.; Chatzichristodoulou, C.; Perry, N. H.; Mogensen, M. B.; Tuller, H. L.; Wachsman, E. D. Chemical Expansion: Implications for Electrochemical Energy Storage and Conversion Devices. *Annu. Rev. Mater. Res.* **2014**, *44*, 205−239.

(23) Sheth, J.; Chen, D.; Kim, J. J.; Bowman, W. J.; Crozier, P. A.; Tuller, H. L.; Misture, S. T.; Zdzieszynski, S.; Sheldon, B.; Bishop, S. Coupling of Strain, Stress, and Oxygen Non-Stoichiometry in Thin Film $Pr_{0.1}Ce_{0.9}O_{2-\delta}$. *Nanoscale* **2016**, *8*, 16499−16510.

(24) Hu, Z.; Kaindl, G.; Ogasawara, H.; Kotani, A.; Felner, I. Ln-4f/ligand-2p covalence in BaLnO3 and Cs3LnF7 (Ln=Ce, Pr, Tb). *Chem. Phys. Lett.* **2000**, *325*, 241−250.

(25) De Souza, R. A.; Gunkel, F.; Hoffmann-Eifert, S.; Dittmann, R. Finite-Size versus Interface-Proximity Effects in Thin-Film Epitaxial $SrTiO_3$. *Phys. Rev. B: Condens. Matter Mater. Phys.* **2014**, *89*, 241401.

(26) Grieshammer, S.; Martin, M. Influence of Defect Interactions on the Free Energy of Reduction in Pure and Doped Ceria. *J. Mater. Chem. A* **2017**, *5*, 9241−9249.

(27) Gopal, C. B.; Van De Walle, A. Ab Initio Thermodynamics of Intrinsic Oxygen Vacancies in Ceria. *Phys. Rev. B: Condens. Matter Mater. Phys.* **2012**, *86*, 134117.

(28) Sutton, J. E.; Beste, A.; Overbury, S. H. Origins and Implications of the Ordering of Oxygen Vacancies and Localized Electrons on Partially Reduced CeO_2(111). *Phys. Rev. B: Condens. Matter Mater. Phys.* **2015**, *92*, 144105.

(29) Esch, F.; Fabris, S.; Zhou, L.; Montini, T.; Africh, C.; Fornasiero, P.; Comelli, G.; Rosei, R. Electron Localization Determines Defect Formation on Ceria Substrates. *Science* **2005**, *309*, 752−755.

(30) Jerratsch, J. F.; Shao, X.; Nilius, N.; Freund, H. J.; Popa, C.; Ganduglia-Pirovano, M. V.; Burow, A. M.; Sauer, J. Electron Localization in Defective Ceria Films: A Study with Scanning-Tunneling Microscopy and Density-Functional Theory. *Phys. Rev. Lett.* **2011**, *106*, 246801.

(31) Bishop, S. R.; Tuller, H. L.; Kuru, Y.; Yildiz, B. Chemical Expansion of Nonstoichiometric $Pr_{0.1}Ce_{0.9}O_{2-\delta}$: Correlation with Defect Equilibrium Model. *J. Eur. Ceram. Soc.* **2011**, *31*, 2351−2356.

(32) Chatzichristodoulou, C.; Hendriksen, P. V.; Hagen, A. Defect Chemistry and Thermomechanical Properties of $Ce_{0.8}Pr_xTb_{0.2-x}O_{2-\delta}$. *J. Electrochem. Soc.* **2010**, *157*, B299−B307.

(33) Lee, W.; Han, J. W.; Chen, Y.; Cai, Z. H.; Yildiz, B. Cation Size Mismatch and Charge Interactions Drive Dopant Segregation at the Surfaces of Manganite Perovskites. *J. Am. Chem. Soc.* **2013**, *135*, 7909−7925.

DOI: 10.1021/acs.chemmater.7b05129
Chem. Mater. 2018, 30, 2600−2606

(34) Sun, L.; Marrocchelli, D.; Yildiz, B. Edge Dislocation Slows down Oxide Ion Diffusion in Doped CeO_2 by Segregation of Charged Defects. *Nat. Commun.* **2015**, *6*, 6294.
(35) Kubacki, J.; Kajewski, D.; Koehl, A.; Wojtyniak, M.; Dittmann, R.; Szade, J. X-Ray Absorption and Resonant Photoemission Studies of Mn Doped $SrTiO_3$ epitaxial Films. *Radiat. Phys. Chem.* **2013**, *93*, 123−128.
(36) Kumigashira, H.; Kobayashi, D.; Hashimoto, R.; Chikamatsu, A.; Oshima, M.; Nakagawa, N.; Ohnishi, T.; Lippmaa, M.; Wadati, H.; Fujimori, a.; Ono, K.; Kawasaki, M.; Koinuma, H. Inherent Charge Transfer Layer Formation at $La_{0.6}Sr_{0.4}FeO_3/La_{0.6}Sr_{0.4}MnO_3$ Heterointerface. *Appl. Phys. Lett.* **2004**, *84*, 5353.
(37) Tsuchiya, T.; Kawamura, K.; Namiki, W.; Furuichi, S.; Takayanagi, M.; Minohara, M.; Kobayashi, M.; Horiba, K.; Kumigashira, H.; Terabe, K.; Higuchi, T. Resonant Photoemission and X-Ray Absorption Spectroscopies of Lithiated Magnetite Thin Film. *Jpn. J. Appl. Phys.* **2017**, *56*, 04CK01.
(38) Kim, J. J.; Bishop, S. R.; Thompson, N. J.; Chen, D.; Tuller, H. L. Investigation of Nonstoichiometry in Oxide Thin Films by Simultaneous *in Situ* Optical Absorption and Chemical Capacitance Measurements: Pr-Doped Ceria, a Case Study. *Chem. Mater.* **2014**, *26*, 1374−1379.
(39) Nenning, A.; Opitz, A. K.; Rameshan, C.; Rameshan, R.; Blume, R.; Hävecker, M.; Knop-Gericke, A.; Rupprechter, G.; Klötzer, B.; Fleig, J. Ambient Pressure XPS Study of Mixed Conducting Perovskite-Type SOFC Cathode and Anode Materials under Well-Defined Electrochemical Polarization. *J. Phys. Chem. C* **2016**, *120*, 1461−1471.
(40) Mueller, D. N.; Machala, M. L.; Bluhm, H.; Chueh, W. C. Redox Activity of Surface Oxygen Anions in Oxygen-Deficient Perovskite Oxides during Electrochemical Reactions. *Nat. Commun.* **2015**, *6*, 6097.
(41) Bowman, W. J.; March, K.; Hernandez, C. A.; Crozier, P. A. Measuring Bandgap States in Individual Non-Stoichiometric Oxide Nanoparticles Using Monochromated STEM EELS: The Praseodymium-Ceria Case. *Ultramicroscopy* **2016**, *167*, 5−10.
(42) Whaley, J. a.; McDaniel, A. H.; El Gabaly, F.; Farrow, R. L.; Grass, M. E.; Hussain, Z.; Liu, Z.; Linne, M. a.; Bluhm, H.; McCarty, K. F. Note: Fixture for Characterizing Electrochemical Devices in-Operando in Traditional Vacuum Systems. *Rev. Sci. Instrum.* **2010**, *81*, 086104.

DOI: 10.1021/acs.chemmater.7b05129
Chem. Mater. 2018, 30, 2600−2606